

## FINDING THE FIRST COSMIC EXPLOSIONS II: CORE-COLLAPSE SUPERNOVAE

DANIEL J. WHALEN<sup>1,2</sup>, CANDACE C. JOGGERST<sup>2</sup>, CHRIS L. FRYER<sup>3</sup>, MASSIMO STIAVELLI<sup>4</sup>, ALEXANDER HEGER<sup>5</sup> AND DANIEL E. HOLZ<sup>6</sup>*Draft version January 12, 2020*

## ABSTRACT

Understanding the properties of Pop III stars is prerequisite to elucidating the nature of primeval galaxies, the chemical enrichment and reionization of the early IGM, and the origin of supermassive black holes. While the primordial IMF remains unknown, recent evidence from numerical simulations and stellar archaeology suggests that some Pop III stars may have had lower masses than previously thought, 15 - 50  $M_{\odot}$  in addition to 50 - 500  $M_{\odot}$ . The detection of Pop III supernovae by *JWST*, *WFIRST* or the *TMT* could directly probe the primordial IMF for the first time. We present numerical simulations of 15 - 40  $M_{\odot}$  Pop III core-collapse SNe done with the Los Alamos radiation hydrodynamics code RAGE. We find that they will be visible in the earliest galaxies out to  $z \sim 10 - 15$ , tracing their star formation rates and in some cases revealing their positions on the sky. Since the central engines of Pop III and solar-metallicity core-collapse SNe are quite similar, future detection of any Type II supernovae by next-generation NIR instruments will in general be limited to this epoch.

*Subject headings:* early universe – galaxies: high-redshift – stars: early-type – supernovae: general – radiative transfer – hydrodynamics – shocks

## 1. INTRODUCTION

The first stars are crucial to the formation of primeval galaxies, the chemical enrichment of the early IGM, the initial stages of cosmological reionization, and the origin of supermassive black holes. Unfortunately, because they lie beyond the reach of current ground and space based instruments there are not yet any observational constraints on their properties. The early numerical simulations of Pop III stars suggest that they form in isolation, one per halo, in  $10^5 - 10^6 M_{\odot}$  dark matter halos at  $z \sim 20 - 30$  and are very massive, 100 - 500  $M_{\odot}$  (Bromm et al. 1999; Abel et al. 2000, 2002; Bromm et al. 2002; Nakamura & Umemura 2001). Usually, such stars drive most of the baryons from their halos in strong ionized flows that create diffuse H II regions with  $n \sim 0.1 - 1 \text{ cm}^{-3}$  (Whalen et al. 2004; Kitayama et al. 2004; Alvarez et al. 2006; Abel et al. 2007; Wise & Abel 2008). Pop III stars are not thought to lose much mass over their lifetimes because there are no line-driven winds in their metal-free atmospheres (Kudritzki 2000; Vink et al. 2001; Baraffe et al. 2001; Ekström et al. 2008).

There is growing evidence that some Pop III stars may be less massive than previously thought. Recent, more extensive ensembles of numerical simulations have found many halos with central collapse rates consistent with 20

- 60  $M_{\odot}$  for the final mass of the star (O’Shea & Norman 2007) and that a fraction of the halos form binaries in this mass range (Turk et al. 2009). New simulations of Pop III protostellar accretion disks suggest that they were prone to fragmentation into as many as a dozen smaller stars (Stacy et al. 2010; Clark et al. 2011; Smith et al. 2011; Greif et al. 2011, 2012). Preliminary models also suggest that ionizing UV breakout from primordial protostellar disks limits the masses of some Pop III stars to  $\sim 40 M_{\odot}$  (Hosokawa et al. 2011; Stacy et al. 2011) (although also see Tan & McKee 2004; McKee & Tan 2008).

While these new models are important steps forward they cannot predict the final masses of primordial stars. For example, the fragmentation of Pop III protostellar disks has only been followed out to a few centuries, far short of the time required to build up a massive star, and many of the fragments in these models are later found to merge with the central object instead of becoming stars themselves. Thus, it is not clear if a small swarm of less massive stars forms or a single, very massive star is created, albeit through protracted clumpy accretion. Clumpy accretion may also keep the protostar puffed up and cool, allowing it to reach much higher masses before evaporating its accretion disk than in the Hosokawa et al. (2011) models. Because no simulation realistically bridges the gap between the formation and fragmentation of the accretion disk and its destruction up to a Myr later, they cannot yet constrain the Pop III initial mass function (IMF).

There have been attempts to determine the masses of the first stars by comparing the cumulative nucleosynthetic yield of their supernovae (SNe) to the fossil abundance record, the chemical abundances measured in ancient, dim extremely metal-poor (EMP) stars out in the Galactic halo (e.g. Beers & Christlieb 2005; Frebel et al. 2005). Pop III stars from 15 - 40  $M_{\odot}$  die in core collapse (CC) SN explosions and 140 - 260  $M_{\odot}$  stars ex-

<sup>1</sup> McWilliams Fellow, Department of Physics, Carnegie Mellon University, Pittsburgh, PA 15213

<sup>2</sup> T-2, Los Alamos National Laboratory, Los Alamos, NM 87545

<sup>3</sup> CCS-2, Los Alamos National Laboratory, Los Alamos, NM 87545

<sup>4</sup> Space Telescope Science Institute, 3700 San Martin Drive, Baltimore, MD 21218

<sup>5</sup> School of Physics and Astronomy, University of Minnesota, Minneapolis, MN 55455

<sup>6</sup> Enrico Fermi Institute, Department of Physics, and Kavli Institute for Cosmological Physics, University of Chicago, Chicago, IL 60637, USA

plode as far more energetic pair instability (PI) SNe (Heger & Woosley 2002) (although the lower mass limit for PI SNe has recently dropped down to  $65 M_{\odot}$  for rotating progenitors – Chatzopoulos & Wheeler 2012). Joggerst et al. (2010) (hereafter JET10) found that the chemical yields of 15 -  $40 M_{\odot}$  Pop III SNe are a good match to the abundances observed in a sample of  $\sim 130$  EMP stars (Cayrel et al. 2004; Lai et al. 2008), and that such stars may have been responsible for much of the chemical enrichment of the primeval IGM. This, together with the failure to detect the distinctive odd-even nucleosynthetic imprint of PI SNe in EMP stars to date, has led some to conclude that Pop III stars could not have been very massive. However, second-generation stars may have been enriched by the ashes of the first PI SNe to metallicities well above those targeted by surveys thus far (Karlsson et al. 2008), so such conclusions are premature. In sum, while stellar archaeology has revealed some insights into the first stellar populations it has not yet placed firm constraints on their masses.

Observations of primordial SNe could directly probe the Pop III IMF for the first time because in principle they can be detected at great distances and distinguish between low mass and high mass progenitors. Until now, calculations of Pop III SN light curves and spectra have been confined to PI SNe to determine if they can be detected by future SN 1a missions ( $4 < z < 6$ , Scannapieco et al. 2005) or by the *James Webb Space Telescope* (*JWST*, Gardner et al. 2006) during the era of reionization ( $6 < z < 15$ , Kasen et al. 2011; Pan et al. 2011) or at  $z \sim 30$  (Wise & Abel 2005; Hummel et al. 2011). Simulations of Pop III PI SN light curves have also been applied to PI candidates in the local universe such as SN 2007bi (Gal-Yam et al. 2009; Young et al. 2010). Most recently, radiation hydrodynamical models of Pop III PI SN light curves and spectra by Whalen et al. (2012c,b) showed for the first time that these explosions will be visible out to  $z \sim 30$  with *JWST* and  $z \sim 15 - 20$  in all-sky near infrared (NIR) surveys such as the *Wide-Field Infrared Survey Telescope* (*WFIRST*) or the *Wide-Field Imaging Surveyor for High-Redshift* (*WISH*). However, no calculation to date has addressed detection thresholds in redshift for Pop III CC SNe, whose numbers may be greater than those of PI SNe at early epochs.

We present radiation hydrodynamical simulations of light curves and spectra for 15 -  $40 M_{\odot}$  Pop III explosions done with the Los Alamos RAGE and SPECTRUM codes. In § 2 we describe our grid of explosion models and how we post process them to obtain light curves and spectra. In § 3 we examine blast profiles and spectra for Pop III CC SNe in detail, and in § 4 we compute their near infrared (NIR) light curves and detection thresholds in redshift. In § 5 we conclude.

## 2. NUMERICAL ALGORITHM

We adopt the models in JET10 for our grid of light curve simulations because they span the range of progenitor masses, structures and explosion energies expected for such stars and because their elemental yields are a good match to those in the fossil abundance record. We calculate light curves and spectra in four stages. First, 15 -  $40 M_{\odot}$  Pop III stars are evolved through all stages of stable nuclear burning and then exploded in the Kepler code. Each explosion is then mapped onto a 2D adaptive

mesh refinement (AMR) grid in the CASTRO code and evolved until just before the shock reaches the surface of the star to capture internal mixing prior to breakout. We then spherically average our CASTRO profiles onto 1D AMR grids in RAGE and evolve them out to 4 months, after which the ejecta dims below observability. Finally, we post process our RAGE profiles with the SPECTRUM code to construct light curves and spectra with detailed atomic opacity sets.

### 2.1. Kepler

We use the 1D Lagrangian stellar evolution code Kepler (Weaver et al. 1978; Woosley et al. 2002) to evolve the progenitors from the beginning of the main sequence to the onset of collapse of their iron cores. The explosions are then artificially triggered by a piston at a constant Lagrangian mass coordinate that advances through the star with a specified radial history. The SNe are evolved through all nuclear burning ( $\sim 100$  s after the explosion) and then the simulations are halted, well before the shock exits the He shell and any reverse shocks form in which instabilities might develop. We follow energy production with a 19-isotope network until oxygen is depleted from the core and with a 128-isotope quasi-equilibrium network thereafter. Stellar rotation is approximated by a semi-convective mixing parameter.

As in JET10, we consider two progenitor metallicities ( $Z = 0$  and  $10^{-4} Z_{\odot}$  denoted by  $z$  and  $u$ , respectively), three explosion energies ( $E_{\text{ex}} = 0.6, 1.2$ , and  $2.4$  B designated by B, D, and G, respectively, where  $1 \text{ B} = 1 \text{ Bethe} = 10^{51} \text{ erg}$ ), and three progenitor masses (15, 25, and  $40 M_{\odot}$ ), a total of 18 models. Thus, model z15G is the  $2.4 \text{ B}$  explosion of a zero-metallicity  $15 M_{\odot}$  Pop III star. We use only one rotation rate from that study ( $R = 5$ , where  $R$  is defined in § 3 of JET10) because it was found that the rate of rotation had little effect on the degree of mixing during the explosion. In contrast to the  $u$ - and  $z$ -series  $150 - 250 M_{\odot}$  stars in Whalen et al. (2012b),  $u$ -series  $15 - 40 M_{\odot}$  Pop III stars die as compact blue giants and  $z$ -series stars die as red supergiants.

We refer our readers to § 2 of JET10 for further details on our Kepler models, such as our numerical mesh, explosion triggers, and use of semi-convective mixing as a proxy for rotation.

### 2.2. CASTRO

As in JET10, we map our Kepler explosion profiles onto a 2D axisymmetric grid in the new CASTRO code (Almgren et al. 2010) and evolve the shock up to the edge of the star in mass coordinate. CASTRO is a multidimensional Eulerian AMR code with a high order, unsplit Godunov hydrodynamics scheme. We follow the same 27 elements from hydrogen to zinc as in JET10 and include the gravity of the compact remnant, which JET10 and others have shown to be crucial to both fallback and mixing in Pop III CC explosions (Zhang et al. 2008). Radiation transport is not necessary in this stage of our calculations because photon mean free paths in the star prior to breakout are so short that they are simply advected through the star by the fluid flow. We do account for the contribution of photons to pressure in the equation of state (EOS). Our models also include energy deposition due to radioactive decay of  $^{56}\text{Ni}$  in the ejecta, as described by equation 4 in JET10.

The JET10 models show that mixing is mostly complete by the time the shock reaches the surface of the star, so elemental mass fractions are realistically distributed in radius and angle in our profiles when we spherically average them and map them into RAGE. We halt the CASTRO simulation when the shock is no less than 100 photon mean free paths  $\lambda_p$  from the edge of the star:

$$\lambda_p = \frac{1}{\kappa\rho}, \quad (1)$$

where  $\kappa$  is the opacity due to Thomson scattering from electrons, taken to be  $0.288 \text{ gm cm}^2$ , and  $\rho$  is the density just ahead of the shock inside the star.

This intermediate step in CASTRO allows us to capture how heavy elements that have built up in the star are mixed in the initial stages of the SN without resorting to full 2D radiation transport models in RAGE. Such calculations, while tractable, would require too much time for a grid of models as large as ours and are not necessary because photon transport does not affect mixing. Mixing determines the order in which emission and absorption lines appear in the spectra over time. If metal lines appear soon after shock breakout in a Pop III SN they would be a clear signature of a core-collapse event because only in such explosions can mixing dredge these elements up from deep inside the star. Intermediate modeling in 2D is not needed for PI SN light curves because mixing is not vigorous enough to bring elements from the core up to the photosphere of the explosion at early times (Joggerst & Whalen 2011).

We refer our readers to § 2 of JET10 for further details on our CASTRO numerical mesh, boundary conditions, gravity scheme, EOS, AMR refinement criteria, and energy deposition due to  $^{56}\text{Ni}$  decay.

### 2.3. RAGE

We evolve the shock through the outer layers of the star, its surface, and then out into the surrounding medium with the radiation hydrodynamics code RAGE (Gittings et al. 2008). RAGE (Radiation Adaptive Grid Eulerian) is an AMR radiation hydrodynamics code that combines a second-order conservative Godunov hydro scheme with grey or multigroup flux-limited diffusion to model strongly radiating flows in 1D, 2D, or 3D. RAGE uses atomic opacities compiled from the extensive LANL OPLIB database<sup>7</sup> (Magee et al. 1995) and can evolve multimaterial flows with several options for the EOS. We describe the physics implemented in our RAGE models in Frey et al. (2012) (hereafter FET12): multi-species advection, 2-temperature (2T) grey flux-limited diffusion, and energy deposition due to the radioactive decay of  $^{56}\text{Ni}$  (Fryer et al. 2009). We note that 2T radiation transport, in which radiation and matter temperatures are evolved separately, better models shock breakout and its aftermath than previous 1T models of SN explosions. We exclude gravity from our RAGE calculations because JET10 showed that fallback onto the central remnant is over before breakout and that its gravity does not strongly affect the shock after it reaches the surface of the star. We evolve mass fractions for the same 27 elements as in CASTRO.

<sup>7</sup> <http://aphysics2/www.t4.lanl.gov/cgi-bin/opacity/tops.pl>

#### 2.3.1. Model Setup

We spherically-average 2D densities, velocities, temperatures and mass fractions for the explosion, the star, and the circumstellar envelope from CASTRO onto a 50,000 zone 1D spherical AMR mesh in RAGE. Since we do not evolve radiation energy densities in CASTRO, we initialize them in RAGE by assuming that

$$E_{\text{rad}} = aT^4, \quad (2)$$

where  $a$  is the radiation constant and  $T$  is the gas temperature in CASTRO. Also, we construct the specific internal energy ( $\text{erg gm}^{-1}$ ) from  $T$  from

$$E_{\text{gas}} = \frac{3}{2}RT, \quad (3)$$

where  $R = 8.314 \times 10^7 \text{ erg K}^{-1}$  is the ideal gas constant. The initial radius of the shock varies from  $4.1 \times 10^{13}$  to  $1.3 \times 10^{14} \text{ cm}$  in the z-series and  $2.04 \times 10^{12}$  to  $4.77 \times 10^{12} \text{ cm}$  in the u-series. Our root grid at setup has a resolution of  $8.0 \times 10^8 \text{ cm}$  and an outer boundary at  $4.0 \times 10^{14} \text{ cm}$  for the z-series and a resolution of  $1.0 \times 10^9 \text{ cm}$  and an outer boundary at  $5.0 \times 10^{13} \text{ cm}$  in the u-series. We allow up to five levels of refinement in both the initial interpolation of the profiles onto the setup grid and later throughout the simulation. Our setup guarantees that all important features in the profiles are resolved by at least 10 grid points and can be subsampled by up to 32 times more points if necessary. We ensure that the explosion is spanned by at least 5000 zones at shock breakout so that the photosphere of the shock is fully resolved; failure to do so can lead to underestimates of luminosity during post-processing.

We impose reflecting and outflow boundary conditions on the fluid and radiation flows at the inner and outer boundaries of the mesh, respectively. When the calculation is launched, Courant times are initially short due to high temperatures, large velocities and small cell sizes. To speed up the simulation and to accommodate the expansion of the ejecta, we periodically resample the profiles onto a larger mesh as the explosion grows. Each regrid significantly increases the time step on which the model evolves. We remap just the explosion itself, excluding any medium beyond the shock, and then graft the original environment that lies beyond this radius onto the shock on the new grid. We apply the same criteria in choosing a new root grid as in the original problem setup: any important density or velocity structure must be resolved by at least 10 mesh zones and be sampled by up to 32 times more zones as needed, and at least 5000 coarse grid zones are allocated to the blast after breakout. The outer boundary of the final largest mesh in our models is  $5.0 \times 10^{16} \text{ cm}$ , the greatest distance the ejecta can propagate in four months.

#### 2.3.2. Circumstellar Envelope

The ambient media of  $z \sim 30$  and  $z \sim 10 - 15$  Pop III PI SNe are quite different because the former occur in small cosmological halos and the latter go off in primeval galaxies. Even low-mass Pop III stars can photoevaporate minihalos (Whalen et al. 2008), and so at  $z \gtrsim 20$  most die in diffuse relic H II regions with  $n \sim 0.1 \text{ cm}^{-3}$ .



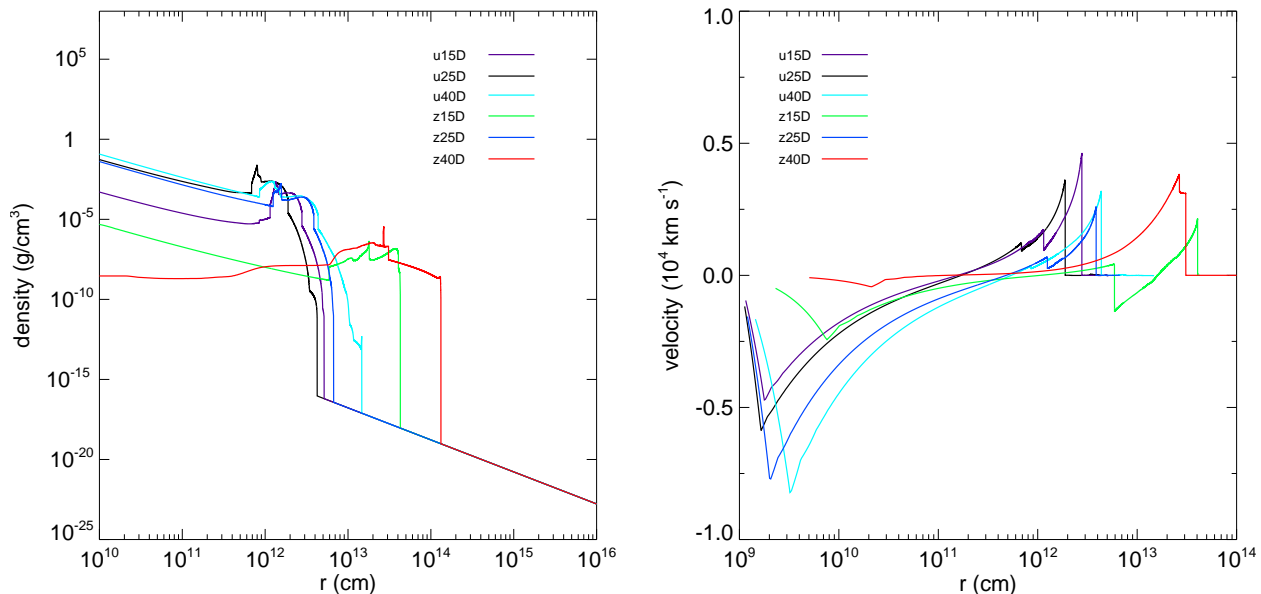


FIG. 1.— Kepler profiles for the shock, the star and its surrounding envelope for both u- and z-series Pop III CC SNe as initialized in RAGE. Left: densities. Right: velocities.

Local densities in  $z \sim 15$  protogalaxies are less well understood but are likely higher. In either case, if the star sheds a wind it will determine the density profile closest to the star. When considering PI SNe, Whalen et al. (2012b) allowed for the possibility that massive Pop III progenitors have modest winds in addition to being surrounded by a diffuse H II region. However, 15 - 40  $M_{\odot}$  Pop III stars are less likely to drive strong winds given their lower surface temperatures, luminosities, and the fact that stars in this mass range today manifest only weak winds, even at solar metallicities. Consequently, in this study we join a very low-mass wind profile to the surface of the star:

$$\rho_W(r) = \frac{\dot{m}}{4\pi r^2 v_W}, \quad (4)$$

where  $\dot{m}$  is the mass loss rate of the wind and  $v_W$  is its speed. The mass loss rate is just

$$\dot{m} = \frac{M_{tot}}{t_{MSL}}, \quad (5)$$

where  $M_{tot}$  and  $t_{MSL}$  are the total mass loss and main sequence lifetime of the star, respectively. We take  $M_{tot}$  to be 0.01  $M_{\odot}$ ,  $v_W$  to be 1000 km s $^{-1}$ , and H and He mass fractions to be 76% and 24%, respectively. We extend the wind from the surface of the star to the outer boundary of the mesh in RAGE. We assume that the wind has enough time to establish a free-streaming region on the grid and that any bubbles blown by the wind are carried far beyond the reach of the ejecta prior to the SN. As in Whalen et al. (2012b), for simplicity the wind surrounding the star is assumed to be neutral. This is true of stars that die as red supergiants, but not for blue giants, which likely ionize their envelopes. Our u-series light curves and spectra should therefore be taken as lower limits. We show initial density and velocity profiles for our blast models in RAGE in Figure 1.

## 2.4. SPECTRUM

To calculate a spectrum from a RAGE profile, we first map its densities, temperatures, velocities and mass fractions onto a 2D grid in the Los Alamos SPECTRUM code. SPECTRUM performs a direct sum of the luminosity of every fluid element in this discretized profile to compute the total flux emitted by the ejecta along the line of sight at every wavelength. This procedure is described in FET12, and it accounts for Doppler shifts and time dilation due to the relativistic expansion of the ejecta. SPECTRUM also calculates the intensities of emission lines and the attenuation of flux along the line of sight, thereby capturing both limb darkening and absorption lines imprinted on the flux by intervening material in the ejecta and wind.

Gas densities, velocities, mass fractions and radiation temperatures from the finest levels of refinement on the RAGE AMR grid are first extracted and ordered by radius into separate files, with one variable in each file. Because of limitations on machine memory and time, we map only a subset of these points onto the SPECTRUM grid. We sample the RAGE radiation energy density profile inward from the outer boundary to determine the position of the radiation front, where  $aT^4$  rises above 1.0 erg/cm $^3$ . We next find the radius of the  $\tau = 20$  surface by integrating the optical depth due to Thomson scattering inward from the outer boundary, taking  $\kappa_{Th}$  to be 0.288 for H and He gas at primordial composition. This is the greatest depth from which radiation can escape from the ejecta, since the minimum total opacity the photons would encounter is that due to just  $e^-$  scattering.

The extracted gas densities, velocities, temperatures and species mass fractions are then interpolated onto a 2D grid in  $r$  and  $\theta$  in SPECTRUM whose inner boundary is that of the RAGE mesh and whose outer boundary is 10 $^{18}$  cm. One hundred uniform zones in log radius are assigned from the center of the grid to the  $\tau = 20$  surface, and the region between the  $\tau = 20$  surface and the edge of

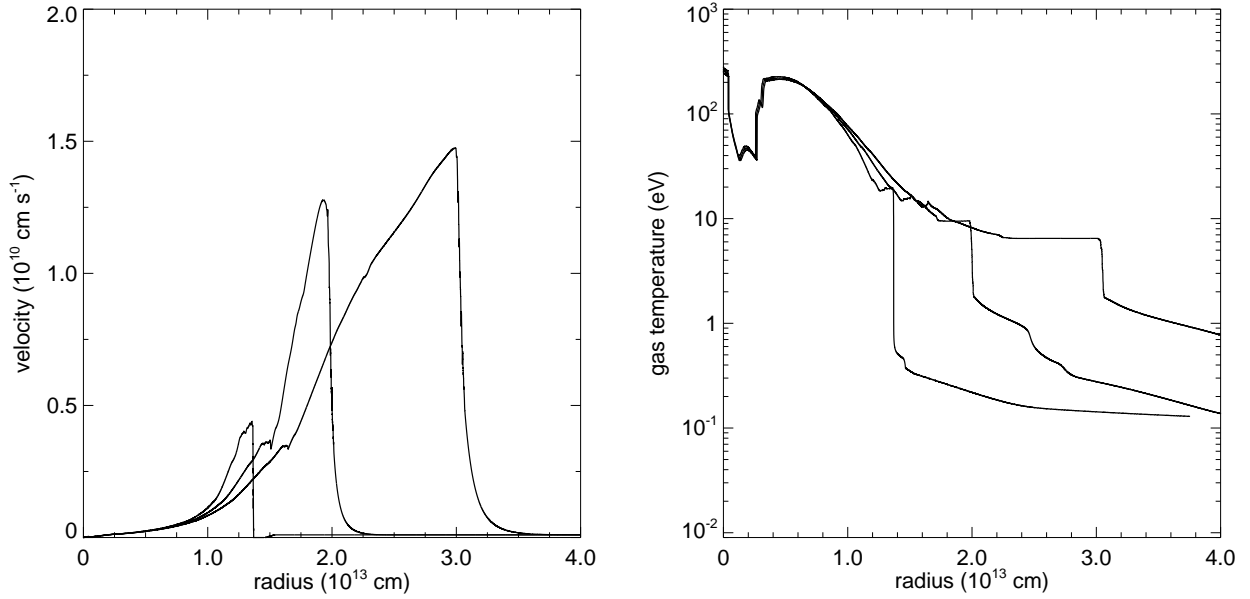


FIG. 2.— Shock breakout in the u40G (compact blue giant) run. Left panel: from left to right, velocities at  $1.81 \times 10^4 \text{ s}$ ,  $1.87 \times 10^4 \text{ s}$  and  $1.93 \times 10^4 \text{ s}$ . Right panel: gas temperatures at the same times.

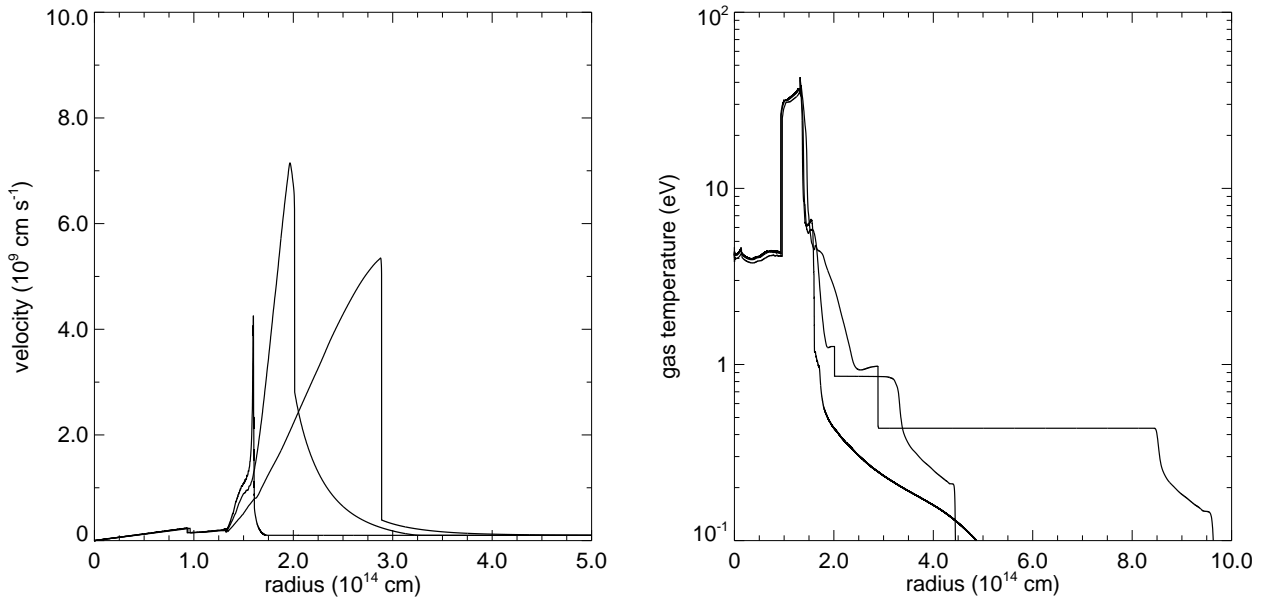


FIG. 3.— Shock breakout in the z40G (red supergiant) run. Left panel: from left to right, velocities at  $3.91 \times 10^5 \text{ s}$ ,  $3.97 \times 10^5 \text{ s}$  and  $4.14 \times 10^5 \text{ s}$ . Right panel: gas temperatures at the same times.

the radiation front is partitioned into 5000 uniform zones in radius. The wind between the front and the outer edge of the grid is divided into one hundred uniform zones in log radius, for a total of 5200 radial bins. The data within each of these new radial bins is mass-averaged to guarantee that the SPECTRUM grid captures very sharp features from the original RAGE profile. The grid is uniformly divided into 160 bins in  $\mu = \cos \theta$  from -1 to 1. Our mesh fully resolves regions of the flow from which photons can escape the ejecta and only lightly samples those from which they cannot.

The sum of the luminosities over all wavelengths in one spectrum yields the bolometric luminosity of the SN at that moment. Many such luminosities computed over a range of times constitutes the light curve of the explosion. We cover shock breakout with 50 spectra uniformly spaced in time and the rest of the light curve with 200 spectra that are logarithmically distributed in time out to 4 months. Each SPECTRUM calculation requires 3 - 6 hours on 32 processors on LANL platforms.

### 3. BLAST PROFILES, LIGHT CURVES AND SPECTRA

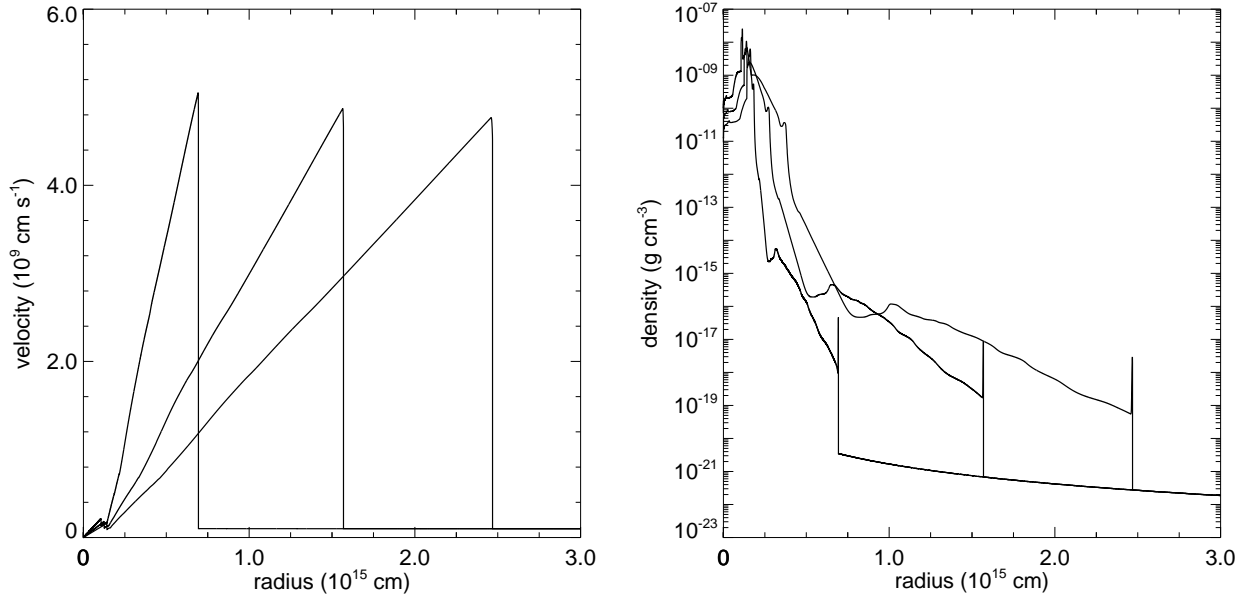


FIG. 4.— The freely expanding u40G SN at intermediate times. Left panel: from left to right, velocities at  $4.96 \times 10^5$  s,  $6.80 \times 10^5$  s, and  $8.74 \times 10^5$  s. Right panel: densities at the same times.

Hydrodynamical profiles for shock breakout are shown for the fiducial cases u40G, a blue giant progenitor, and z40G, a red supergiant progenitor, in Figures 2 and 3. The reverse shock in the z40G velocity profile in Figure 1, which vigorously mixes the interior of the star prior to breakout (Figure 5 of Joggerst et al. 2010), is gone by the time the shock reaches the surface of the star at  $3.91 \times 10^5$  s. With no reverse shock there is no further Rayleigh-Taylor mixing, and the metals are essentially frozen in mass coordinate as the ejecta expands. Our procedure for spherically averaging 2D CASTRO mass fractions to approximate their radial distribution in 1D in RAGE therefore captures all mixing in the explosion. The SN is not visible to an external observer before breakout because electrons between the surface and the shock scatter the photons.

When the shock breaks through the surface of the star its velocity abruptly doubles (z40G) or triples (u40G). As photons stream free from the shock they blow off the outer layers of the star. The breakout transient is visible as the flat plateau in gas temperature that moves ahead of the ejecta. This plateau traces the leading edge of the radiation front. The height of the plateau is the temperature to which the radiation pulse heats the gas as it passes through it, not the temperature of the fireball itself, which is much higher. The u40G shock is much hotter than the z40G shock at breakout ( $\sim 100$  eV vs. 10 eV) because it has broken out of a much more compact star and done less  $PdV$  work on its surroundings. Consequently, the radiation front initially heats the wind to 20 eV in u40G but to only 1 eV in z40G. As the shock expands its spectrum softens, and the temperature of the gas behind the radiation front falls over time: from 20 eV to 8 eV in u40G from  $1.81 \times 10^4$  s to  $1.93 \times 10^4$  s and from 1.2 eV to 0.4 eV in z40G from  $3.91 \times 10^5$  s to  $4.14 \times 10^5$  s.

In both explosions, shock breakout coincides with radiation breakout because the moderate wind density at

the surface of the star cannot confine the radiation front. As both shocks descend the  $r^{-2}$  wind gradient, the u40G SN accelerates but the z40G SN speeds up and then decelerates. The u40G shock continues to accelerate even though ambient densities are 1000 times higher at the surface of the star because the explosion is much hotter and the shock is more radiatively driven than the much cooler z40G shock. Soon after breakout, both SNe assume self-similar free expansion velocity profiles and homologously expand, as we show in Figure 4 for u40G. This self-similar expansion continues until the end of the simulations at 4 months. Eventually, spherical dilution of the ejecta renders the SN transparent, and it enters the nebular phase. At this stage, fluid elements in the ejecta may no longer remain in radiation equilibrium with their neighbors so the true opacity may deviate from the OPLIB opacities, which assume local thermodynamic equilibrium (LTE). Also, the Kirchhoff-Planck relation (equation 6 of Frey et al. 2012) may not fully hold in the SPECTRUM code. There may therefore be some inaccuracy in our spectra at late times, but these events are only visible in the NIR at much earlier stages of the explosion, as we later show.

### 3.1. Light Curves / Spectra

We show bolometric luminosities for our Pop III CC SNe in Figure 5. Peak luminosities at shock breakout vary from  $8 \times 10^{44}$  to  $1.5 \times 10^{46}$  erg s $^{-1}$  in the z-series and from  $3 \times 10^{44}$  to  $5 \times 10^{45}$  erg s $^{-1}$  in the u-series. At early times the light curve is powered primarily by the conversion of kinetic energy into thermal energy by the shock, so for a given progenitor mass the peak luminosities increase with explosion energy. They peak at earlier times with greater  $E$  because the shock reaches the surface of the star in less time. Breakout also generally happens later with more massive stars because they have greater radii in both series, with the exception of the  $25 M_{\odot}$  star because it dies with the smallest radius,

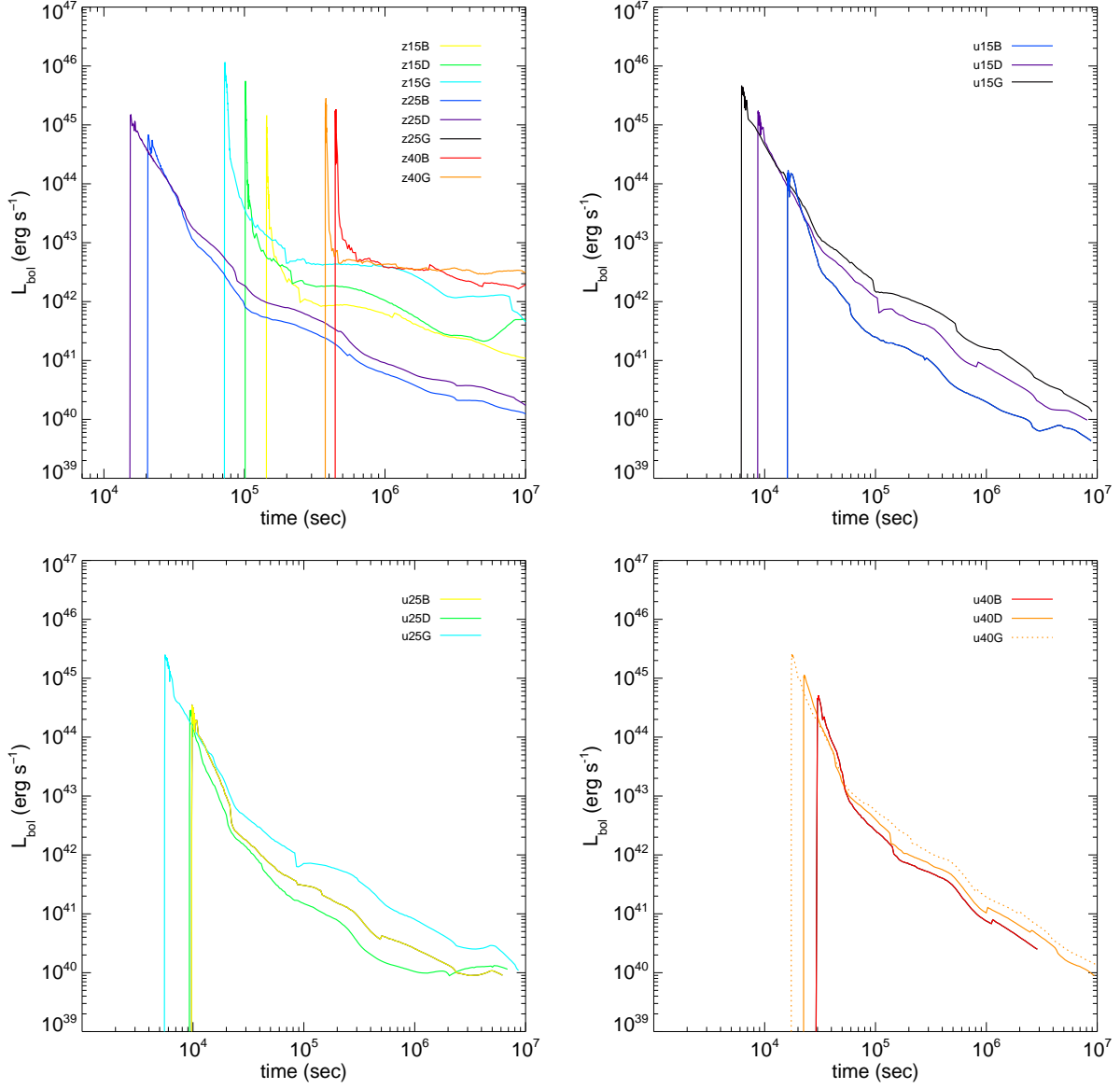


FIG. 5.— Bolometric light curves for 17 Pop III CC SNe in the source frame. Upper left: all eight z-series light curves (red supergiant progenitors). Upper right, lower left and lower right are u15, u25, and u40 (blue giant progenitor) light curves, respectively.

as shown in Figure 1. For a given progenitor mass and  $E$ , u-series SNe are somewhat less luminous than z-series SNe, and this is due to a tradeoff between shock temperature at breakout and the radius of the star:

$$L = 4\pi\epsilon r^2 \sigma T^4. \quad (6)$$

Here,  $\sigma$  is the Stefan-Boltzmann constant,  $\epsilon$  is the greybody correction to the blackbody luminosity assumed for the shock ( $\epsilon \sim 0.1$ ), and  $T$  is the temperature of the shock at the  $\tau_{Th} = 1$  surface, where  $\kappa_{Th} = 0.288$ . The red z-series stars have radii 10 - 30 times greater than u-series stars of equal mass but their shocks have lower temperatures at breakout because they must do more  $PdV$  work before crashing through the surface of the star. Their respective temperatures are evident in their spectra at breakout, which we show in Figure 6. The u40G model has much more spectral energy below 10 Å than z40G at

breakout because the fireball has a much higher temperature. The duration of the breakout transient is governed by the light-crossing time of the star and is 10 - 30 times greater in the z-series than in the u-series because of their larger radii.

As the shock expands it cools, and its emission at later times is powered by the radioactive decay of  $^{56}\text{Ni}$ . The duration of this emission can be approximated by the radiation diffusion timescales in the ejecta:

$$t_d \sim \kappa^{\frac{1}{2}} M_{ej}^{\frac{3}{4}} E^{-\frac{3}{4}}, \quad (7)$$

where  $M_{ej}$  is the mass of the ejecta,  $\kappa$  is the average opacity of the ejecta, and  $E$  is the explosion energy. The u-series SNe dim after about 3 months but the z-series explosions exhibit much more extended emission reminiscent of Type IIp SNe, whose progenitors are also thought to be red supergiants. In particular, the z40 series remain

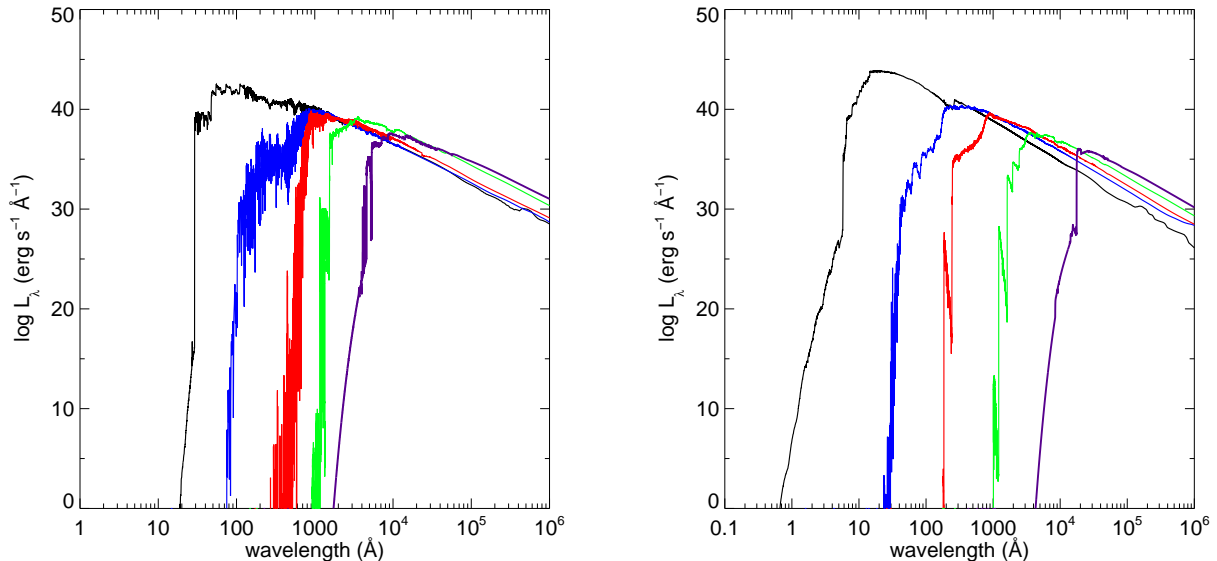


FIG. 6.— Spectral evolution of the fireball. Right: z40G at  $3.92 \times 10^5$  s (black),  $5.55 \times 10^5$  s (blue),  $1.49 \times 10^6$  s (red),  $8.66 \times 10^6$  s (green) and  $2.95 \times 10^7$  s (purple). Left: u40G at  $1.87 \times 10^4$  s (black),  $6.82 \times 10^4$  s (blue),  $2.06 \times 10^5$  s (red),  $1.21 \times 10^6$  s (green) and  $9.69 \times 10^6$  s (purple).

above  $10^{42}$  erg s $^{-1}$  for up to 300 days. However, because the shock cools over time, the region of its spectrum that is redshifted into the NIR in the observer frame dims below detection limits well before 1 year, as we discuss below.

We show the evolution of the z40G and u40G spectra in Figure 6. Unlike with much more energetic Pop III PI SNe, the outer regions of the ejecta and the envelope are never fully ionized, so they always blanket the spectrum with absorption lines at the short wavelength limit. As the shock expands and cools its surrounding envelope imposes more lines on the spectrum and continuum emission at long wavelengths slowly rises. The flux at longer wavelengths increases with time because the ejecta cools and its surface area grows. From these profiles, it is clear that fitting a blackbody profile to a bolometric luminosity to approximate a spectrum can lead to serious overestimates of flux at short wavelengths, because it erroneously reinstates luminosity that is actually removed by line blanketing. This caveat is especially pertinent to detection thresholds for high-redshift SNe because flux from this region of the spectrum is a principal component of the NIR signal of the explosion in the observer frame. The collision of the shock with a realistic circumstellar envelope (which sets its temperature) and the opacity of the ejecta and envelope also crucially shape the spectra in the source frame, and thus the NIR light curve in the observer frame.

#### 4. POP III CC SN DETECTION THRESHOLDS

We calculate NIR light curves for our SNe with the photometry code developed by Su et al. (2011). Each spectrum is redshifted before removing the flux that is absorbed by intervening neutral hydrogen along the line of sight according to the method of Madau (1995). The spectrum is then dimmed by the required cosmological factors. We linearly interpolate the least sampled data between the input spectrum and filter curve to model the light curve in a given filter.

#### 4.1. NIR Light Curves

At every redshift for each supernova, we calculate the NIR signal in *JWST* NIRCams filters above and below the Lyman limit to find the filter in which the SN is brightest. As in Whalen et al. (2012c), we find that the CC SNe in our study are most luminous just redward of 1216 Å in the source frame at the redshifts we consider. We show NIR light curves for z-series and u-series SNe at  $z = 7, 10$  and 15 in Figures 7 and 8. The NIRCams photometry limit is AB magnitude 32, and so six of the eight z-series SNe will be visible for 20 - 600 days at  $z = 7$  but only one of the u-series explosions, u40G, will be visible, and only for  $\sim 30$  days. Five of the z-series SNe will be visible at  $z = 10$ : z15B for less than 1 day, z15D for 75 days, z15G for 220 days, z40B for 275 days and z40G for over 400 days. At  $z = 15$  the z15G SN is visible for 250 days and the z40B and z40G explosions can be seen for 300 days. The peak in emission for all the SNe advances to later times and is broader at earlier epochs because of cosmological redshifting. For a given mass, the NIR luminosity increases with the explosion energy.

Shock breakout is not visible from earth in any of these SNe because the x-rays and hard UV in the transient are absorbed by neutral H at high redshift. The flux that is redshifted into the NIR varies much more rapidly (on timescales of  $\sim 100$  days) than the bolometric luminosity (3 - 7 years) in the observer frame because the spectra evolve as the fireball expands. The light curves rise more rapidly than they fall, so they are most recognizable as transients in their early stages. However, given *JWST* survey times of 1 - 5 years, it will be possible to identify these events as SNe at any stage above detection threshold. Because they are much dimmer than Pop III PI SNe and because  $z \sim 7$  galaxies will be more luminous than  $z \sim 10 - 15$  protogalaxies, some Pop III CC SNe may be somewhat more challenging to discriminate from their host galaxies (with which they likely overlap in color-color space). However, they will still be more luminous



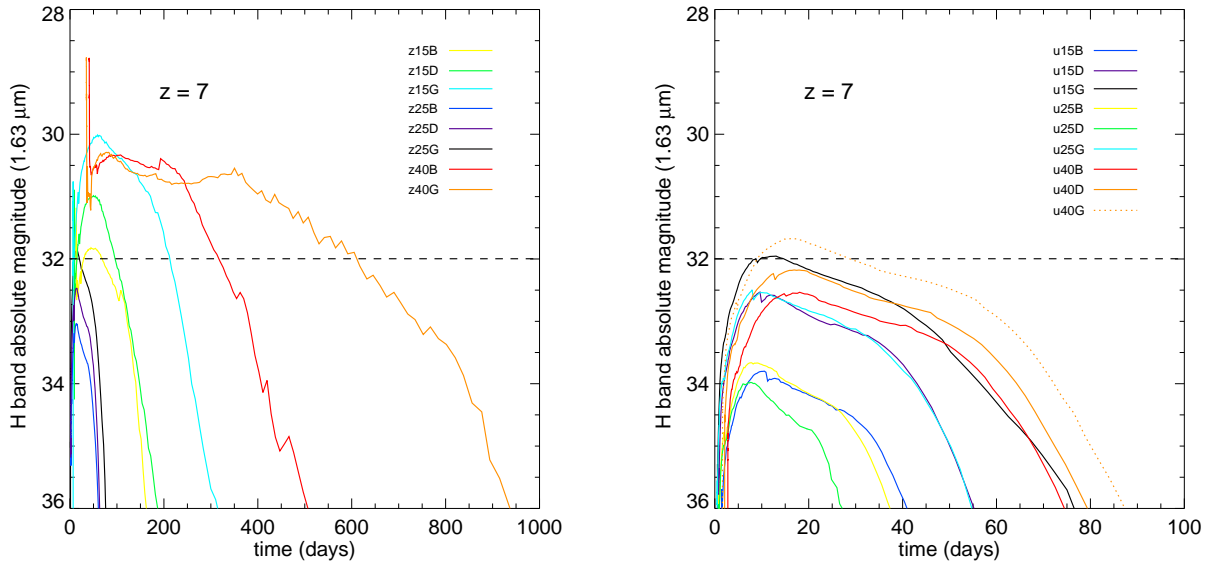


FIG. 7.— NIR light curves for  $z = 7$  Pop III CC SNe at  $1.63 \mu\text{m}$  in the observer frame. Left: z-series. Right: u-series

than most galaxies of that epoch and may be much more frequent than PI SNe if baryons in some metal-free halos collapse and fragment into small swarms of stars rather than a few very massive ones, as the latest numerical simulations suggest.

The prospects for detecting Pop III CC SNe with *JWST* at  $z \gtrsim 10$  are better than those for PI SNe (e.g., Hummel et al. 2011) because of their higher rates, but they will be too dim to be found in future all-sky NIR surveys such as *Euclid*, whose detection limit is AB magnitude 24 at  $2 \mu\text{m}$ , or *WFIRST* and *WISH*, whose photometry limits will be AB magnitude 27 at  $2.2 \mu\text{m}$ . They also will fall below the detection threshold in the Y-band centered at  $1.0 \mu\text{m}$  for the *Large Synoptic Survey Telescope* (*LSST*) and the *Panoramic Survey Telescope & Rapid Response System* (*Pan-STARRS*), whose photometry limits will be at most AB magnitude 25 and 27, respectively. Our SPECTRUM calculations show that these SNe will be even dimmer in the optical in *LSST* and *Pan-STARRS* because of extinction by the IGM at high redshift. We note that while we have considered only Pop III CC SNe, our detection limits hold for progenitors of any metallicity. The central engine of the explosion depends mostly on the entropy profile of the inner  $3 - 4 M_{\odot}$  of the star, which does not vary strongly with metallicity (Chieffi & Limongi 2004; Woosley & Heger 2007) (see also Figure 1 in Whalen & Fryer 2012). The light curves and spectra of CC SNe at higher metallicities should therefore be bracketed by those of our compact blue giant and red supergiant Pop III progenitor stars.

##### 5. CONCLUSION

Although direct detections of Pop III CC SNe will not probe the very first stellar populations, they will reveal the properties of stars in  $z \sim 10 - 15$  galaxies and trace their formation rates and early galactic chemical evolution in general. Furthermore, because they will likely be brighter than most primitive galaxies of that era, explosions of low-mass Pop III stars (and indeed any CC explosion) will reveal the existence of primeval galaxies on the sky that might otherwise escape detection by *JWST* or future ground-based 30-meter class telescopes. We

note that while we have considered explosion energies of  $0.6 - 2.4 \text{ Be}$ , higher energies may be possible for some CC SNe and would be visible at even higher redshifts.

There are also scenarios in which CC explosions can produce luminosities that rival those of PI explosions that could be visible at much earlier epochs. For example, if the shock collides with a dense shell ejected during a luminous blue variable (LBV) outburst prior to the SN, an extremely bright event in the UV can result that could be detected above  $z \sim 15$  (e.g. Smith & McCray 2007; Smith et al. 2007; van Marle et al. 2010; Moriya et al. 2010). We are now studying the observational signatures of these superluminous Pop III Type IIn SNe (Whalen et al. 2012a). There may also be hypernovae, very energetic explosions of  $40 - 60 M_{\odot}$  stars with energies of  $10^{52}$  erg that are intermediate to those of CC and PI SNe. This kind of explosion, whose existence is inferred in part from the elemental abundances imprinted on a few of the most metal-poor stars found to date (Iwamoto et al. 2005), could be detected at redshifts that bridge those at which CC and PI SNe can be found,  $15 < z < 20$ . We are also calculating light curves and spectra for such events.

Strong gravitational lensing by massive galaxies and clusters at  $z \sim 0 - 1$  could magnify flux from Pop III supernovae, improving prospects for their detection (Rydberg et al. 2012). The probability that flux from a Pop III SN would be boosted in an all-sky survey and its magnification depend on the event rate on the entire sky at a given redshift. We have performed preliminary Markov Chain Monte Carlo ray-tracing calculations that suggest that the probability that a  $z \sim 20$  event is lensed is  $\sim 1 - 5\%$  for flux boosts of  $2 - 5$ . Much higher magnifications ( $10 - 300$ ) are possible near the edges of massive clusters but the search volumes and probabilities of encountering high- $z$  SNe are much smaller. We continue to study strong lensing of  $z \sim 20$  events, the highest redshifts ever attempted, in order to assess its potential to discover primeval SNe and galaxies.

Can later stages of the SN remnant be detected? Whalen et al. (2008) found that most of the energy of

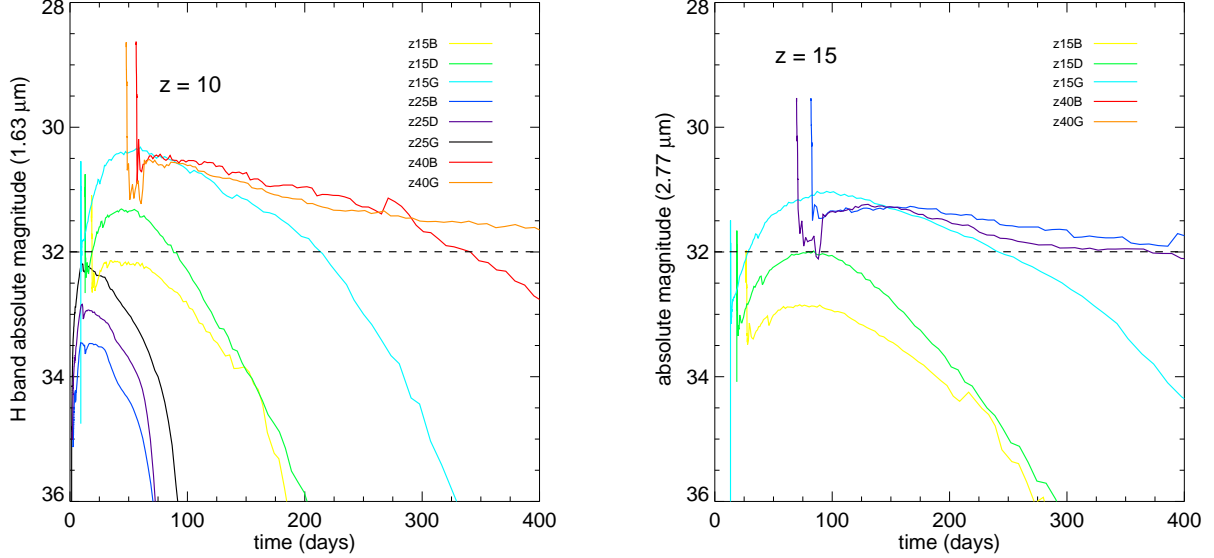


FIG. 8.— NIR light curves for  $z$ -series SNe at  $1.63\ \mu\text{m}$  (left,  $z = 10$ ) and at  $2.77\ \mu\text{m}$  (right,  $z = 15$ ) in the observer frame.

15 and  $40\ M_{\odot}$  Pop III SNe is eventually radiated away as H and He lines as the remnant sweeps up and shocks pristine gas. At lower redshifts this energy would instead be lost to fine structure cooling by metals. In either case, the emission is too diffuse, redshifted and drawn out over time to be detected by any upcoming instruments. Also, unlike PI SNe, CC SNe deposit little of their energy into the cosmic microwave background (CMB) by inverse Compton scattering at  $z \sim 20$  (Kitayama & Yoshida 2005; Whalen et al. 2008), and even less at lower redshifts because the density of CMB photons falls with cosmological expansion. Consequently, early populations of low-mass Pop III SNe will probably not impose excess power on the CMB at small scales (Oh et al. 2003). For the same reason it will probably not be possible to directly image Sunyaev-Zeldovich fluctuations from individual Pop III CC SN remnants with the *Atacama Cosmology Telescope* or the *South Pole Telescope*.

Although their event rates make it unlikely that Pop III CC SNe will be detected in absorption at 21 cm at  $z > 10$ , new calculations reveal that enough synchrotron emission from their remnants is redshifted into the 21 cm band above  $z \sim 10$  to be directly detected by the *Square Kilometer Array (SKA)* (Meiksin & Whalen 2012). Somewhat more energetic hypernovae could be detected by existing facilities such as the *Extended Very-*

*Large Array (eVLA)* and *eMERLIN*. Whether by direct detection or by their footprint on cosmic backgrounds, these ancient supernovae will soon open a new window on the  $z \sim 10 - 15$  universe.

DJW is grateful for helpful discussions with Edo Berger, Ranga Ram Chary, Daniel Kasen, Avi Loeb, Pete Roming and the many participants at First Stars and Galaxies: Challenges for the Next Decade, held at UT Austin March 8 - 11, 2010. He also acknowledges support from the Bruce and Astrid McWilliams Center for Cosmology at Carnegie Mellon University. AH was supported by the US Department of Energy under contracts DE-FC02-01ER41176, FC02-09ER41618 (SciDAC), and DE-FG02-87ER40328. MS thanks Marcia Rieke for making available the NIRCam filter curves and was partially supported by NASA JWST grant NAG5-12458. DEH acknowledges support from the National Science Foundation CAREER grant PHY-1151836. Work at LANL was done under the auspices of the National Nuclear Security Administration of the U.S. Department of Energy at Los Alamos National Laboratory under Contract No. DE-AC52-06NA25396. All CASTRO, RAGE and SPECTRUM calculations were performed on Institutional Computing (IC) and Yellow network platforms at LANL (Conejo, Lobo and Yellowrail).

## REFERENCES

- Abel, T., Bryan, G. L., & Norman, M. L. 2000, *ApJ*, 540, 39  
—, 2002, *Science*, 295, 93  
Abel, T., Wise, J. H., & Bryan, G. L. 2007, *ApJ*, 659, L87  
Almgren, A. S., Beckner, V. E., Bell, J. B., Day, M. S., Howell, L. H., Joggerst, C. C., Lijewski, M. J., Nonaka, A., Singer, M., & Zingale, M. 2010, *ApJ*, 715, 1221  
Alvarez, M. A., Bromm, V., & Shapiro, P. R. 2006, *ApJ*, 639, 621  
Baraffe, I., Heger, A., & Woosley, S. E. 2001, *ApJ*, 550, 890  
Beers, T. C. & Christlieb, N. 2005, *ARA&A*, 43, 531  
Bromm, V., Coppi, P. S., & Larson, R. B. 1999, *ApJ*, 527, L5  
—, 2002, *ApJ*, 564, 23  
Cayrel, R., Depagne, E., Spite, M., Hill, V., Spite, F., François, P., Plez, B., Beers, T., Primas, F., Andersen, J., Barbey, B., Bonifacio, P., Molaro, P., & Nordström, B. 2004, *A&A*, 416, 1117  
Chatzopoulos, E. & Wheeler, J. C. 2012, *ApJ*, 748, 42  
Chieffi, A. & Limongi, M. 2004, *ApJ*, 608, 405  
Clark, P. C., Glover, S. C. O., Smith, R. J., Greif, T. H., Klessen, R. S., & Bromm, V. 2011, *Science*, 331, 1040  
Ekström, S., Meynet, G., Chiappini, C., Hirschi, R., & Maeder, A. 2008, *A&A*, 489, 685

- Febel, A., Aoki, W., Christlieb, N., Ando, H., Asplund, M., Barklem, P. S., Beers, T. C., Eriksson, K., Fechner, C., Fujimoto, M. Y., Honda, S., Kajino, T., Minezaki, T., Nomoto, K., Norris, J. E., Ryan, S. G., Takada-Hidai, M., Tsangarides, S., & Yoshii, Y. 2005, *Nature*, 434, 871
- Frey, L. H., Even, W., Whalen, D. J., Fryer, C. L., Hungerford, A. L., Fontes, C. J., & Colgan, J. 2012, ArXiv e-prints
- Fryer, C. L., Brown, P. J., Bufano, F., Dahl, J. A., Fontes, C. J., Frey, L. H., Holland, S. T., Hungerford, A. L., Immler, S., Mazzali, P., Milne, P. A., Scannapieco, E., Weinberg, N., & Young, P. A. 2009, *ApJ*, 707, 193
- Gal-Yam, A., Mazzali, P., Ofek, E. O., Nugent, P. E., Kulkarni, S. R., Kasliwal, M. M., Quimby, R. M., Filippenko, A. V., Cenko, S. B., Chornock, R., Waldman, R., Kasen, D., Sullivan, M., Beshore, E. C., Drake, A. J., Thomas, R. C., Bloom, J. S., Poznanski, D., Miller, A. A., Foley, R. J., Silverman, J. M., Arcavi, I., Ellis, R. S., & Deng, J. 2009, *Nature*, 462, 624
- Gardner, J. P., Mather, J. C., Clampin, M., Doyon, R., Greenhouse, M. A., Hammel, H. B., Hutchings, J. B., Jakobsen, P., Lilly, S. J., Long, K. S., Lunine, J. I., McCaughrean, M. J., Mountain, M., Nella, J., Rieke, G. H., Rieke, M. J., Rix, H.-W., Smith, E. P., Sonneborn, G., Stiavelli, M., Stockman, H. S., Windhorst, R. A., & Wright, G. S. 2006, *Space Sci. Rev.*, 123, 485
- Gittings, M., Weaver, R., Clover, M., Betlach, T., Byrne, N., Coker, R., Dendy, E., Hueckstaedt, R., New, K., Oakes, W. R., Ranta, D., & Stefan, R. 2008, *Computational Science and Discovery*, 1, 015005
- Greif, T. H., Bromm, V., Clark, P. C., Glover, S. C. O., Smith, R. J., Klessen, R. S., Yoshida, N., & Springel, V. 2012, *MNRAS*, 424, 399
- Greif, T. H., Springel, V., White, S. D. M., Glover, S. C. O., Clark, P. C., Smith, R. J., Klessen, R. S., & Bromm, V. 2011, *ApJ*, 737, 75
- Heger, A. & Woosley, S. E. 2002, *ApJ*, 567, 532
- Hosokawa, T., Omukai, K., Yoshida, N., & Yorke, H. W. 2011, *Science*, 334, 1250
- Hummel, J., Pawlik, A., Milosavljevic, M., & Bromm, V. 2011, ArXiv e-prints
- Iwamoto, N., Umeda, H., Tominaga, N., Nomoto, K., & Maeda, K. 2005, *Science*, 309, 451
- Joggerst, C. C., Almgren, A., Bell, J., Heger, A., Whalen, D., & Woosley, S. E. 2010, *ApJ*, 709, 11
- Joggerst, C. C. & Whalen, D. J. 2011, *ApJ*, 728, 129
- Karlsson, T., Johnson, J. L., & Bromm, V. 2008, *ApJ*, 679, 6
- Kasen, D., Woosley, S. E., & Heger, A. 2011, *ApJ*, 734, 102
- Kitayama, T. & Yoshida, N. 2005, *ApJ*, 630, 675
- Kitayama, T., Yoshida, N., Susa, H., & Umemura, M. 2004, *ApJ*, 613, 631
- Kudritzki, R. 2000, in *The First Stars*, ed. A. Weiss, T. G. Abel, & V. Hill, 127–+
- Lai, D. K., Bolte, M., Johnson, J. A., Lucatello, S., Heger, A., & Woosley, S. E. 2008, *ApJ*, 681, 1524
- Madau, P. 1995, *ApJ*, 441, 18
- Magee, N. H., Abdallah, Jr., J., Clark, R. E. H., Cohen, J. S., Collins, L. A., Csanak, G., Fontes, C. J., Gauger, A., Keady, J. J., Kilcrease, D. P., & Merts, A. L. 1995, in *Astronomical Society of the Pacific Conference Series*, Vol. 78, *Astrophysical Applications of Powerful New Databases*, ed. S. J. Adelman & W. L. Wiese, 51
- McKee, C. F. & Tan, J. C. 2008, *ApJ*, 681, 771
- Meiksin, A. & Whalen, D. J. 2012, ArXiv e-prints
- Moriya, T., Yoshida, N., Tominaga, N., Blinnikov, S. I., Maeda, K., Tanaka, M., & Nomoto, K. 2010, in *American Institute of Physics Conference Series*, Vol. 1294, *American Institute of Physics Conference Series*, ed. D. J. Whalen, V. Bromm, & N. Yoshida, 268–269
- Nakamura, F. & Umemura, M. 2001, *ApJ*, 548, 19
- Oh, S. P., Cooray, A., & Kamionkowski, M. 2003, *MNRAS*, 342, L20
- O’Shea, B. W. & Norman, M. L. 2007, *ApJ*, 654, 66
- Pan, T., Kasen, D., & Loeb, A. 2011, ArXiv e-prints
- Rydberg, C.-E., Zackrisson, E., Lundqvist, P., & Scott, P. 2012, ArXiv e-prints
- Scannapieco, E., Madau, P., Woosley, S., Heger, A., & Ferrara, A. 2005, *ApJ*, 633, 1031
- Smith, N., Li, W., Foley, R. J., Wheeler, J. C., Pooley, D., Chornock, R., Filippenko, A. V., Silverman, J. M., Quimby, R., Bloom, J. S., & Hansen, C. 2007, *ApJ*, 666, 1116
- Smith, N. & McCray, R. 2007, *ApJ*, 671, L17
- Smith, R. J., Glover, S. C. O., Clark, P. C., Greif, T., & Klessen, R. S. 2011, *MNRAS*, 414, 3633
- Stacy, A., Greif, T. H., & Bromm, V. 2010, *MNRAS*, 403, 45
- , 2011, ArXiv e-prints
- Su, J., Stiavelli, M., Oesch, P., Trenti, M., Bergeron, E., Bradley, L., Carollo, M., Dahlen, T., Ferguson, H. C., Gialaisco, M., Koekemoer, A., Lilly, S., Lucas, R. A., Mobasher, B., Panagia, N., & Pavlovsky, C. 2011, *ApJ*, 738, 123
- Tan, J. C. & McKee, C. F. 2004, *ApJ*, 603, 383
- Turk, M. J., Abel, T., & O’Shea, B. 2009, *Science*, 325, 601
- van Marle, A. J., Smith, N., Owocski, S. P., & van Veelen, B. 2010, *MNRAS*, 407, 2305
- Vink, J. S., de Koter, A., & Lamers, H. J. G. L. M. 2001, *A&A*, 369, 574
- Weaver, T. A., Zimmerman, G. B., & Woosley, S. E. 1978, *ApJ*, 225, 1021
- Whalen, D., Abel, T., & Norman, M. L. 2004, *ApJ*, 610, 14
- Whalen, D., van Veelen, B., O’Shea, B. W., & Norman, M. L. 2008, *ApJ*, 682, 49
- Whalen, D. J., Even, W., Lovekin, C. C., Fryer, C. L., Holz, D. H., Stiavelli, M., & Knight, C. 2012a, *ApJ*, submitted
- Whalen, D. J., Frey, L. H., Even, W., Fryer, C. L., Holz, D. H., Stiavelli, M., Heger, A. H., Hungerford, A. L., & Lovekin, C. C. 2012b, *ApJ*, submitted
- Whalen, D. J. & Fryer, C. L. 2012, *ApJ*, 756, L19
- Whalen, D. J., Fryer, C. L., Holz, D. E., Heger, A., Woosley, S. E., Stiavelli, M., Even, W., & Frey, L. L. 2012c, ArXiv e-prints
- Wise, J. H. & Abel, T. 2005, *ApJ*, 629, 615
- , 2008, *ApJ*, 684, 1
- Woosley, S. E. & Heger, A. 2007, *Phys. Rep.*, 442, 269
- Woosley, S. E., Heger, A., & Weaver, T. A. 2002, *Reviews of Modern Physics*, 74, 1015
- Young, D. R., Smartt, S. J., Valenti, S., Pastorello, A., Benetti, S., Binn, C. R., Bersier, D., Botticella, M. T., Corradi, R. L. M., Harutyunyan, A. H., Hrudkova, M., Hunter, I., Mattila, S., de Mooij, E. J. W., Navasardyan, H., Snellen, I. A. G., Tanvir, N. R., & Zampieri, L. 2010, *A&A*, 512, A70+
- Zhang, W., Woosley, S. E., & Heger, A. 2008, *ApJ*, 679, 639